Supporting Information

Seleno Analogs of Pentlandite (Fe$_{4.5}$Ni$_{4.5}$S$_{8-y}$Se$_y$, Y = 1-6):

Tuning bulk Fe/Ni Sulphoselenides for Hydrogen Evolution

Mathias Smialkowski,[a] Daniel Siegmund [b], Kevinjeorjios Pellumbi,[a] Lars Hensgen,[c] Hendrik Antoni,[d] Martin Muhler[d] and Ulf-Peter Apfel[a,b]*

[a] Inorganic Chemistry I -Bioinorganic Chemistry, Ruhr University Bochum, Universitätsstrasse 150, 44801, Bochum, Germany
[b] Fraunhofer UMSICHT, Osterfelder Str. 3, 46047, Oberhausen, Germany
[c] Tribotecc GmbH, Fleischmarkt 3-5, 1010 Vienna, Austria
[d] Industrial Chemistry, Ruhr University Bochum, Universitätsstrasse 150, 44801, Bochum, Germany

ORCID

Ulf-Peter Apfel: 0000-0002-1577-2420

Daniel Siegmund: 0000-0003-2476-8965

Table of Contents

1. Experimental Part

1.1 General information

Unless otherwise stated, all chemicals were purchased from commercial vendors. Iron (Sigma-Aldrich, 99.99%), Nickel (Riedel-de Haen, 99.8%), Sulfur (Sigma-Aldrich, 99.5-100.5%), Selenium (Sigma-Aldrich, 99.999%) and Iodine (Sigma-Aldrich, 99.9%) were used without any further purification. Sulfuric acid (Alfa Aesar, >95%) was diluted with deionized water purified by Millipore Direct-Q purification system.

1.2 Synthesis of $Fe_{4.5}Ni_{4.5}S_{8-Y}Se_Y$ (Y = 1 - 8). The compounds were synthesized according to previously reported procedures beginning from mixtures of the pure elements.[1,2] Iron, nickel, sulfur and selenium were weighed in the desired ratio and mixed thoroughly by mortar and pistil. The grey powder mixture was then put into a silica glass ampule, which was evacuated for 12 hours. After this, the ampule was sealed conserving the reduced pressure (p = 1.2x10^{-2} mbar). The mixture was heated up to 700°C by a rate of 5 K min^{-1} in a horizontal tubular furnace. This temperature was held for three hours until it was further increased to a final temperature of 1000°C by a rate of 10 K min^{-1}. After 10h of annealing the oven cooled down naturally to room temperature within five hours. The content of the ampule was removed by cracking the vessel and separating the grey product from the quartz glass fragments.

1.3 Growing of $Fe_{4.5}Ni_{4.5}S_{8-Y}Se_Y$ crystals (Y = 0, 1, 4). The obtained product $Fe_{4.5}Ni_{4.5}S_{8-Y}Se_Y$ (Y = 0, 4) was ground to a fine dark-grey powder and a small portion of iodine was added (25 at.%). The mixture was thoroughly ground to obtain a fine homogeneous powder.[3] This was transferred to a silica glass ampule, which was constantly pumped down to reduced pressure of 1.2x10$^-$ mbar for 12 hours. The ampule then was sealed conserving the reduced pressure and the temperature was annealed to 860°C for a minimum of 16 days in a tubular furnace. After this the oven was cooled down to room temperature at a rate of 0.4 K min^{-1}. The obtained crystalline material was used for analysis without necessity of further preparation.

1.4 Electrode fabrication. The synthesized compounds were ground to a fine powder and pressed to a cylindrical pellet with a diameter of 3 mm. The pellet was contacted to a brass rod and both was placed in a PTFE housing. The electrical contact was provided by a conductive two-component glue (Polytec EC 151 L). To cure the glue the electrode was placed in an oven at 60°C for 12h. Afterwards, the electrode surface was polished with 10 µm, 1 µm and 0.3 µm lapping film (3M) to obtain a flat and smooth surface with an area of 0.071 cm^2.

1.5 Electrochemical measurements. The electrochemical measurements were performed using a GAMRY Reference 600 Potentiostat and a three-electrode setup, using as prepared iron-nickel sulfoselenide electrodes as working electrode, Ag/AgCl (conc. KCl or 3M KCl) as reference and a Pt-mesh as counter electrode. All experiments were performed in aqueous 0.5M H_2SO_4 electrolyte solution. The measured potentials were converted to the reversible hydrogen electrode (RHE) according to the equation $E_{RHE}=E_{(Ag/AgCl)}+x+0.059 \cdot pH$ (x = 0.197 mV for sat. KCl, x = 0.210 mV for 3 M KCl). For compensation of the iR drop between the reference and the working electrode the embedded iR drop correction of the potentiostat was used. Prior to the desired electrochemical measurements, electrode conditioning was performed by the help of cyclic voltammetry (10-20 cycles, 100 mV s^{-1}) in the potential range of -0.6 mV to +0.2 mV vs RHE until a stable cyclic voltammogram shape was obtained. Linear sweep voltammetry (LSV) was performed in the potential range between -0.6 mV to +0.0 mV vs RHE scanning with a rate of 5 mV s^{-1}. The electrochemical surface area determined by scanning the non-faradaic range between -0.0 mV to +0.0 mV vs RHE via cyclic voltammetry with rates of 10, 20, 30, 40, 50 and 60 mV s^{-1}, respectively. All long-term measurements were performed at a constantly applied potential of -0.5 mV vs RHE over a period of 20 h. The faradaic efficiencies where determined by injection of gas samples into a modified GC Agilent 7820a and subsequent common correlation of the obtained hydrogen gas concentration to the transmitted charges during the long-term measurements. The obtained currents during all electrochemical measurements were converted to current densities in regard to the geometrical area of the respective working electrode.

1.6 Physical Characterization. Differential scanning calorimetry (DSC) was performed for all synthesized compounds using a NETZSCH STA 449 F3 Jupiter. About 50 mg of sample was weighted into a closed corundum crucible, which was placed inside the oven chamber. The temperature was raised from room temperature up to 1000°C and back by a rate of 10 K min^{-1}. The oven chamber was purged with gaseous nitrogen (N_2). Most of the samples were investigated using a scanning electron microscope (SEM) coupled with electron dispersive x-ray spectroscopy (EDX). Either a Leo (Zeiss) 1530 Gemini FESEM, or a Zeiss Gemini 2 (Merlin) was operated up to a voltage of 20 kV for scanning electron microscopy and 0 - 20 kV for electron dispersive x-ray spectroscopy (EDX). For powder X-ray diffraction (PXRD) a diffractometer from HUBER, equipped with a Molybdenum source (Mo-K_{α}, λ = 0.709 Å) was used. All powder patterns were converted from Molybdenum to Copper radiation via Bragg's Law to ensure comparability with literature known values. Measurements on single crystals were performed either using a STOE IPDS diffractometer or Rigaku XtaLAB Synergy equipped with a HyPix detector (both diffractometers: Mo-K_{α}, λ = 0.71073 Å). The crystals were cooled by a cold N_2-stream throughout the experiment. Structures were solved by direct methods (SHELXS) or intrinsic phasing (SHELXT) and refined against F^2 (SHELXL). The obtained structures are deposited with the joined Cambridge Crystallographic Data Centre/FIZ Karlsruhe deposition service and can be obtained free of charge using the reported deposition numbers. X-ray photoelectron spectroscopy (XPS) measurements were carried out in an ultrahigh vacuum set-up equipped with a monochromatic Al Ka X-ray source (1486.6 eV), operated at 14.5 kV and 35 mA, and a high-resolution Gammadata-Scienta SES 2002 analyser. The base pressure in the measurement chamber was maintained at 10^{-10} mbar. The sample pellets were glued to the holder with carbon tape. The measurements were carried out in the fixed transmission mode with a pass energy of 200 eV, resulting in an overall energy resolution of 0.25 eV. A flood gun was applied to compensate the charging effects. CasaXPS software with pseudo-Voigt Gaussian-Lorentzian function was used for the deconvolution.

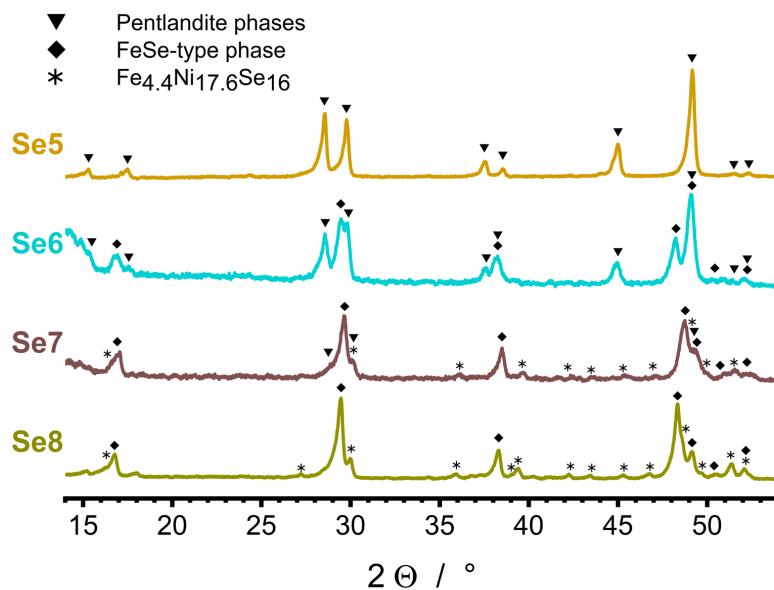## 2. Characterization

2.1 Powder diffraction

*Figure S1: Detailed comparison of powder diffraction patterns of the synthesized materials **Se5** - **Se8**.*

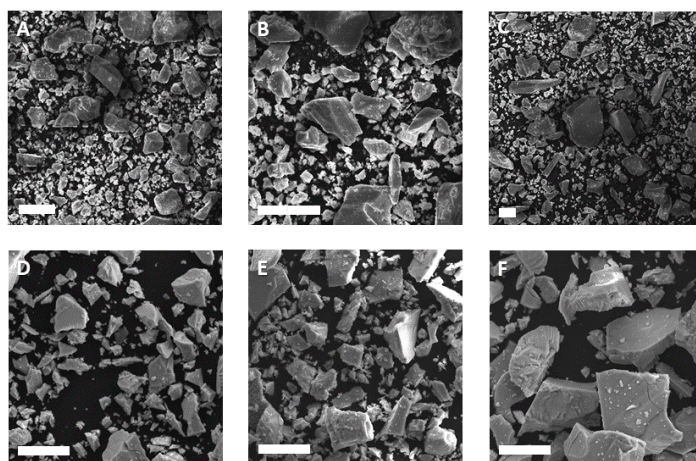### 2.2 Scanning electron microscopy images

*Figure S2: SEM images of the different powdered $Fe_{4.5}Ni_{4.5}S_{8-Y}Se_{Y}$ a) **Pn** (Y=0), b) **Se1** (Y=1), c) **Se2** (Y=2), d) **Se3** (Y=3), e) **Se4** (Y=4) and f) **Se5** (Y=5) with 20 µm scale bars.*

Figure S3 compares the pellet electrode surface of **Se1** before (Fig. S3A) and after 20 h (Fig. S3B) electrolysis at a potential -0.5 V vs RHE. It is obvious that the surface texture and morphology is conserved throughout the experiment. This indicates that the observed activity increase cannot solely be attributed to a growing surface area.
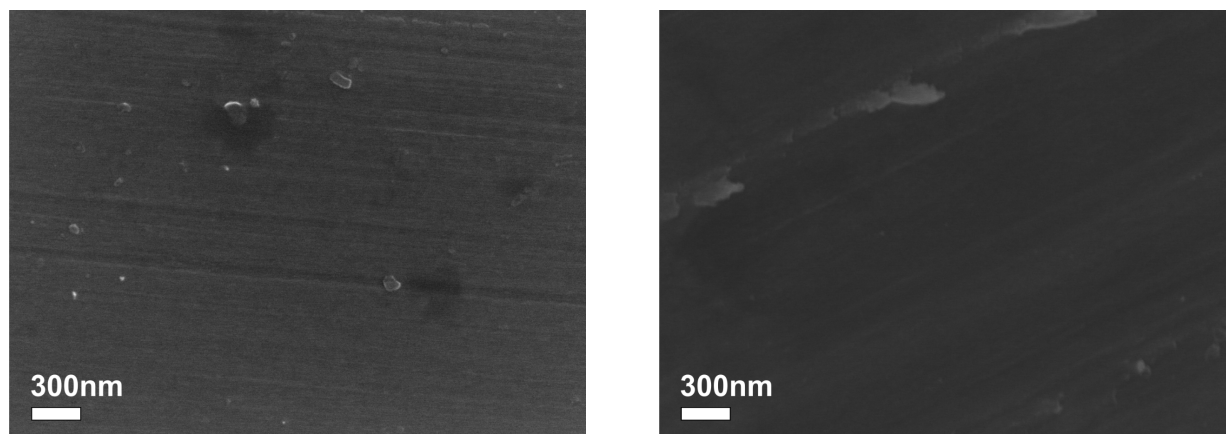

Figure S3: SEM images of a Se1 pellet electrode surface before (A) and after (B) electrolysis.
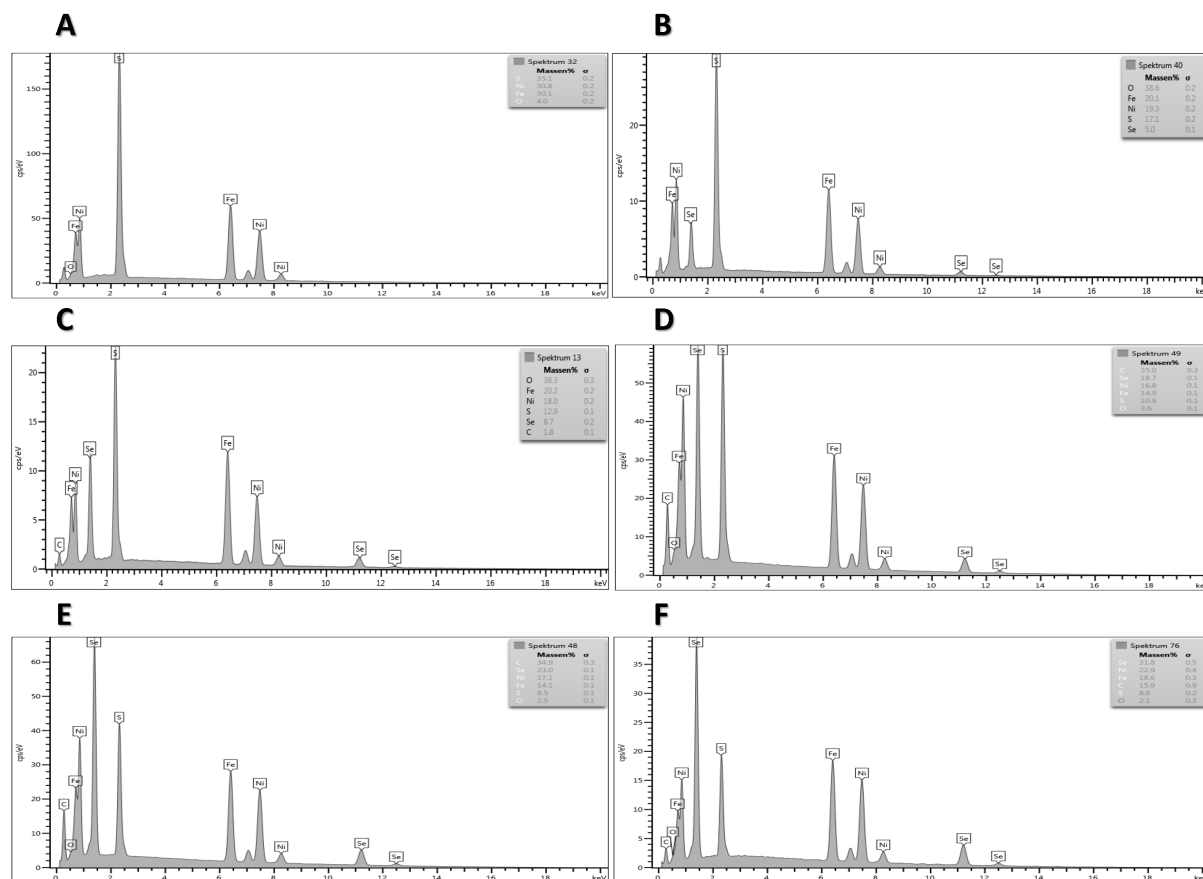
2.3 EDX

*Figure S4: Energy dispersive X-ray scans of $Fe_{4.5}Ni_{4.5}S_{8-Y}Se_Y$ compounds a) **Pn** (Y=0), b) **Se1** (Y=1), c) **Se2** (Y=2), d) **Se3** (Y=3), e) **Se4** (Y=4) and f) **Se5** (Y=5).*

2.4 Crystal structures

Table S1:Summary of crystal data and refinement details.

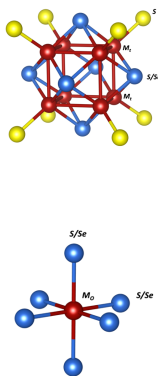| Compound	Pn	Se1	Se4
Empirical formula	$Fe_{15.46} Ni_{20.54} S_{32}$	$Fe_{18.63} Ni_{17.73} S_{28.10} Se_{3.90}$	$Fe_{20.12} Ni_{15.88} S_{17.14} Se_{14.86}$
Formula weight	3095.26	3269.11	3778.87
Temperature [K]	173(2)	103(2)	103(2)
Wavelength [Å]	0.71073	0.71073	0.71073
Crystal system	Cubic	Cubic	Cubic
Space group	Fm-3m	Fm-3m	Fm-3m
Cell constant [Å]	10.1109(12)	10.1234(3)	10.3275(2)
Volume [Å³]	1033.6(4)	1037.48(9)	1101.50(6)
Density [Mg/m³]	4.973	5.232	5.697
Absorption coefficient [mm⁻¹]	15.948	18.784	26.081
F(000)	1489	1553	1747
Theta range	3.490 to 24.946°	3.486 to 30.091°	3.417 to 29.989°
Reflections collected	1829	398	500
Independent reflections	69	86	100
Completeness [%]	97.2	95.8	98.6
Data / restraints/ parameters	69 / 0 / 11	86 / 0 /12	100 / 2 / 13
Goodness-of-fit on F^2	1.255	1.067	1.309
Final R indices [I>2sigma(I)]	R1 = 0.0136, wR2 = 0.0365	R1 = 0.0104, wR2 = 0.0229	R1 = 0.0210, wR2 = 0.0537
R indices (all data)	R1 = 0.0136, wR2 = 0.0365	R1 = 0.0104, wR2 = 0.0229	R1 = 0.0213, wR2 = 0.0538
Deposition number	1896032	1896033	1896034
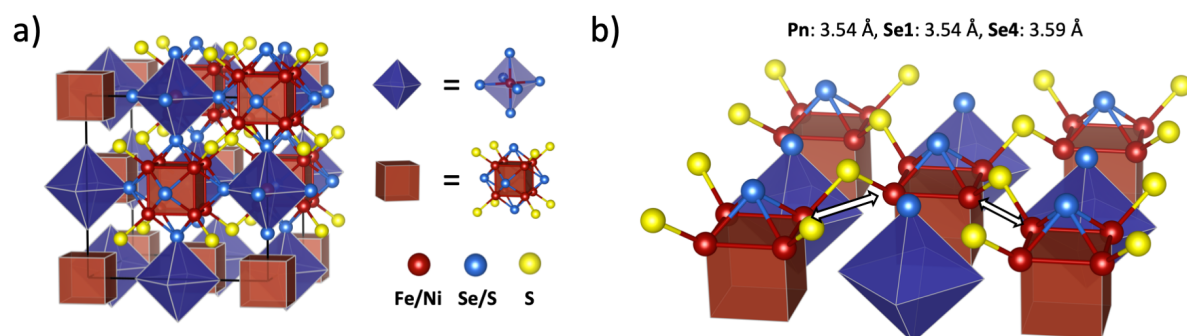
Figure S5: Crystal structure of Pentlandite materials (a) and representation of the metal-metal distance around Wyckoff position 8c (yellow atoms). Atoms below the surface were omitted for clarity (b).

All obtained crystal structures adopt the expected pentlandite structure in space group Fm-3m. Chalcogenes and metal atoms both adopt two distinct crystallographic sites each. Metal atoms can adopt either an octahedral site (site: *4b*, symmetry: m-3m) with 6 coordinating chalcogenes (blue octahedra in Figure S5, chalcogene site: *24e*, symmetry: 4m.m, blue atoms) or a second metal-site, coordinated to 4 chalcogene atoms in a tetrahedral fashion (site: *32f*, symmetry: .3m). Furthermore, the metal atoms in site *32f* form cubic metal clusters (red cubes in Figure S5) which are bridged by the second chalcogene species (yellow atoms, site: *8c*, symmetry: -43m). In **Se1** and **Se4**, this second chalcogene site is mainly occupied by sulphur and believed to be prone to sulphur depletion during electrochemical activation. The resulting vacancies with their metal environment are ascribed to be the main hydrogen adsorption sites (see Figure S3b for visualization of metal-metal distances in this position). The metal clusters are furthermore face-capped by chalcogene species *24e* which represent the edges of the octahedra, thus completing the depicted structure in Figure S4a. Selected bond lengths and angles are presented in table S2.

*Table S2: Selected bond lengths and angles in **Pn**, **Se1** and **Se4**.*

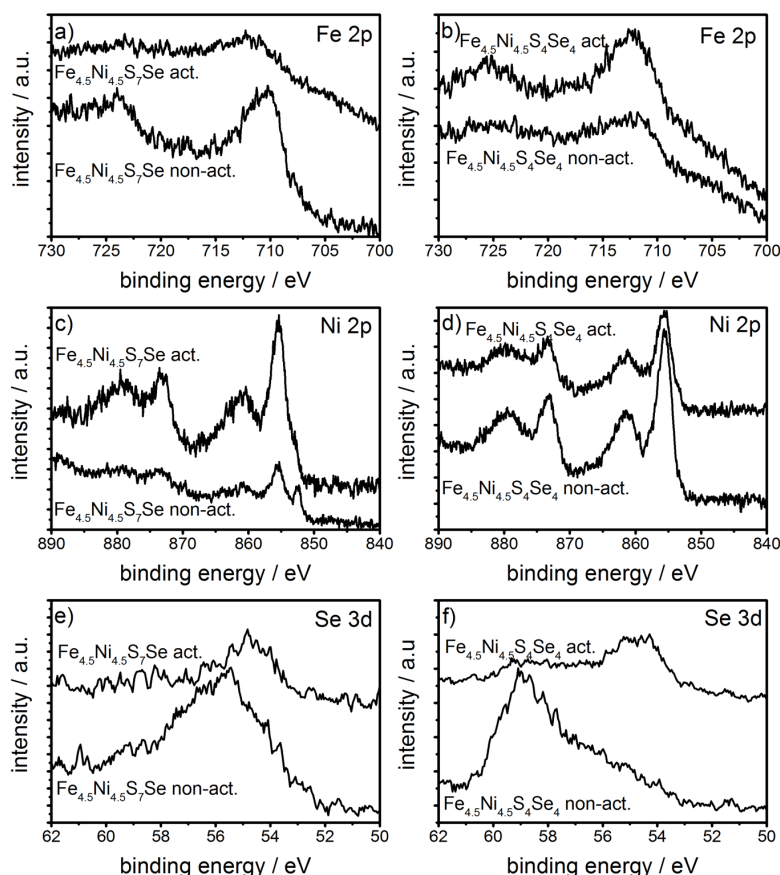|	Pn	Se1	Se4
Distances [Å]			
M_t - M_t	2.555	2.561	2.623
M_t - S/Se	2.259	2.272	2.327
M_t - S	2.166	2.165	2.201
M_O - S/Se	2.421	2.409	2.447
M_O - S	4.378	4.384	4.472
M-M (sulphur depletion site)	3.537	3.536	3.593
Angles [°]			
M_t - S/Se - M_t	68.85	68.60	68.61
S - M_t - S/Se	107.82	107.58	107.58
S/Se - M_t - S/Se	111.07	111.30	111.29
M_o - S/Se - M_t	126.92	127.16	127.15

2.5 X-ray Photoelectron Spectroscopy

*Figure S6: High resolution Fe 2p(a, b), Ni 2p(b, c) and Se 3d(e,f) XP spectra of the **Se1** (a, c, e) and **Se4** (b, d, f) samples before and after activation. The C1s peak binding energy (284.5 eV) was used as reference.*

Figure 3 (see manuscript) shows the high-resolution XP spectra of the Se1 (a) and Se4 (b) samples before and after activation. Peak deconvolution was implemented because the S 2p and Se 3p core-level photoelectrons superpose and to get information about the surface composition with respect to certain species. The peaks considered for deconvolution are Se $3p_{3/2}$ and Se $3p_{1/2}$ at around 160.0 eV and 165.8 eV related to elemental Se(0) and 164.3 eV and 170.1 eV related to Se(IV) in SeO_2. For the sake of clarity only one doublet was fitted at around 161.5 eV and 162.7 eV for the S $2p_{1/2}$ and S $2p_{3/2}$ peaks of various oxysulfide species, denoted as S_x^{2-}.

Besides, some spectra exhibit one doublet at 167.8 and 169.0 eV for the S $2p_{1/2}$ and S $2p_{3/2}$ peaks attributable to sulfate species, probably arising from sulfuric acid residuals. The peak assignment agrees well with literature reported data.[4,5] Table x lists the overall sample composition, determined by the XPS regions. The carbon and oxygen content is rather high because of detected photoelectrons originating from the carbon tape used for pellet fixation. Figure 3a) depicts the change of the respective Se(0) and S_x^{2-} peaks of Se1 after the activation process, with no indication for Se(IV) in both spectra. The amount of sulfur present on the surface decreases from 3.60 to 2.94 at%, indicating that sulfur depletion has occurred. That entails that the selenium content increases from 0.23 to 0.86 at%.

Due to the stoichiometric lower sulfur and higher selenium content of the non-activated Se4 (Figure 3b) sample the surface composition amounts to 1.02 at% sulfide and 1.93 at.% selenium (total), pointing to a surface enrichment of selenium. However, distinct peaks for Se(IV) are predominantly present for the non-activated sample. After activation the Se(IV) content decreases from 1.62 at.% to 0.39 at.%, while the Se(0) content increases from 0.31 to 0.61 indicating that surface reduction has occurred. Again, sulfur depletion is indicated by a decreasing sulfide content from 1.02 at.% to 0.64 at%.

Figure S6. shows high resolution Fe 2p(a, b), Ni 2p(b, c) and Se 3d(e,f) XP spectra of the Se1 (a, c, e) and Se4 (b, d, f) samples before and after activation. From the Fe $2p_{3/2}$ peak (Figure S6a,b) at around 711.7 eV and the Ni $2p_{3/2}$ peak (Figure S6c,d) at 855.4 eV it can be concluded the species appear to be in the oxidized state. Since the XP spectra differences of the main oxidation states (+2 and+3) for Fe and Ni are only marginal and due to the required multiplet fittings for first row transition metals, we refrain from further deconvolution and comments on the exact oxidation states. Moreover, it is hardly possible see any changes comparing the non-activated and activated spectra. Merely the non-activated Se1 sample exhibits a peak at 852.4 eV, attributable to either NiS or metallic Ni residuals from the synthesis, which disappears after activation.

Concerning the Se 3d spectra (Figure S6 e, f) it is particular difficult to draw conclusions because of the low Se content of the Se1 sample, the low cross-section of the Se 3d region and a strong overlap of the Se(0) peak with the Fe 3p peak.[6] However, Figure S6 f) shows a strong peak at 59.0 eV, which can be assigned to Se(IV) in SeO_2 for the non-activated Se4 sample. The peak decrease after activation indicates that Se reduction has occurred, which substantiates the observation from the S 2p region in Figure 3b.

Notably, no Pt was observed via XPS after 20 h electrolysis at potentials of -0.5 V vs RHE.

Table S3: Overall sample surface composition in atomic % measured by XPS. Se1 and Se4 samples before and after activation.

sample	C	S (total)	SO$_4$	S$_x^{2-}$	O	Fe	Ni	Se (total)	Se(0)	Se(IV)
Se1	63.87	4.25	0.65	3.60	27.86	2.54	1.24	0.23	0.23	0.00
Se1(act.)	57.08	2.94	0.00	2.94	31.66	2.30	5.17	0.86	0.86	0.00
Se4	50.52	1.75	0.73	1.02	36.01	3.20	6.58	1.93	0.31	1.62
Se4(act.)	61.34	2.89	2.25	0.64	28.43	1.75	4.59	1.00	0.61	0.39

Table S3: Overall sample surface composition in atomic % measured by XPS. Se1 and Se4 samples before and after activation.

sample	C	S (total)	SO$_4$	S$_x^{2-}$	O	Fe	Ni	Se (total)	Se(0)	Se(IV)

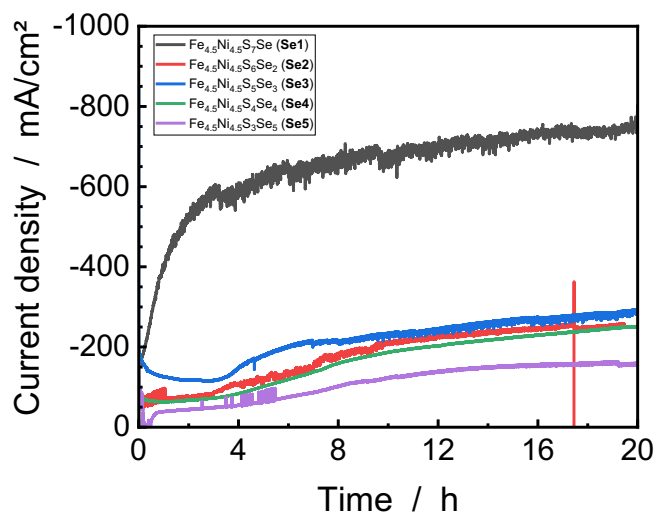# 3. Electrochemical measurements

3.1 Activation

*Figure S7: J-t-curves of **Se1** to **Se5** obtained in 0.5 M H$_2$SO$_4$ at a potential of -0.5 V vs RHE for 20 hours.*

3.2 Electrochemical active surface area

To visualize changes in the electrochemical active surface during the activation process, the electrochemical surface area was determined before and after electrolysis (Fig. S8a,b). For this purpose, CVs were measured in non-catalytically active regions of each catalyst according to the aforementioned procedure. More information on the evaluation of ECSA data on **Pn**-like materials can be found elsewhere.[7] The slopes for the electrochemical active surface area for non-activated electrodes are comparable for all materials tested (Fig. S8c). However, the data show a slight reduction of the ECSA slopes with increasing amount of selenium. This same trend remains for the materials after activation. Notably, the ECSA is smaller for materials revealing a higher selenium-content. Furthermore, the total increase of the ECSA after activation is larger for low selenium-contents suggesting more pronounced changes on the surface of the compounds with low or no selenium-contents. In analogy to our previous observations and the SEM data, this trend further supports the suggested sulfur-depletion mechanism of the materials, which comprehensibly obviously is preferred in compounds revealing a lower selenium content.[1,3,7,8]
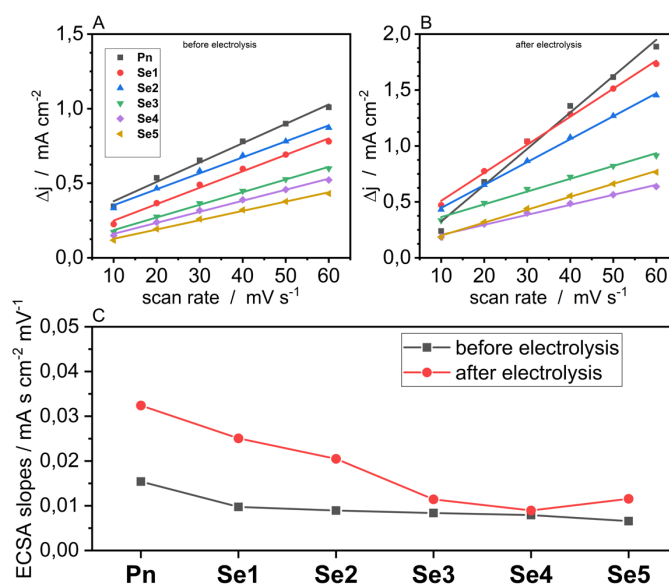

Figure S8: Charging current density differences of the electrodes before (A) and after (B) electrolysis at different scan rates. The slopes of the linear regression of these curves are presented as ECSA slopes in (C) before and after electrolysis.

3.3 Usage of alternative counter electrode materials and different cells

"The possibility that dissolved Pt from the counter electrode contributes to the decrease of the overpotential also needs to be considered for long-lasting electrochemical experiments."[8] To investigate the influence of the counter electrode on the activation process of the seleno-pentlandite materials, the aforementioned activation experiments were repeated with a non-Pt containing glassy carbon electrode. As shown in the Figure S9, the increase of activity of **Se1** is comparable for Pt-counter electrode and "glassy carbon" counter electrodes within the first 2 hours. Experiments for a significant longer time were not possible due to constant disintegration of the glassy carbon electrode. We assume that the CE disintegration, as well as the changes occurring to the electrochemical environment during the experiment result in an overall lowered current density. However, the observation of similar activity increase for both experiments gave confidence that the activation is not a result of Pt-deposition. To further support our claim we again performed the experiment in presence of a Pt-CE but separated by a Nafion®-membrane using a H-type cell setup, fresh electrolyte and new electrodes. Notably, a similar trend as observed for Pt in a one compartment cell is observed. This also leads to the conclusion that the activation is independent of the presence of Platinum and is a result of an intrinsic material change.
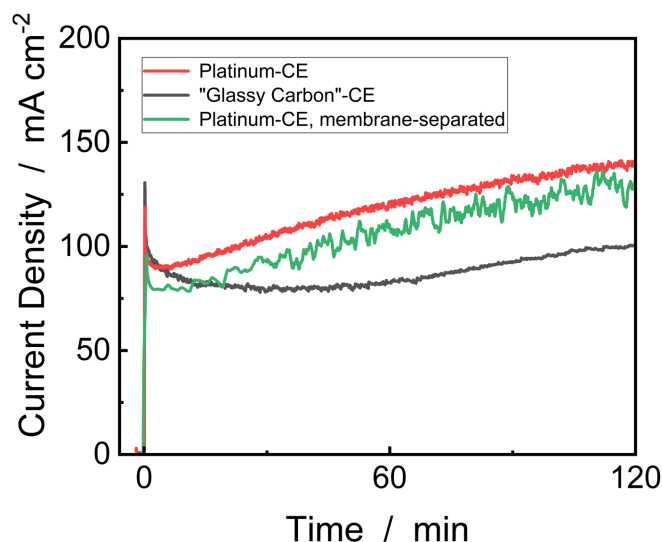

*Figure S9: Chronoamperometric measurements of **Se1** performed in as described setups equipped with a platinum counter electrode (red curve), an "glassy carbon" counter electrode (black) and with a membrane-separated platinum counter electrode (green curve) at an applied potential of -0.5V vs RHE in 0.5M H₂SO₄.*
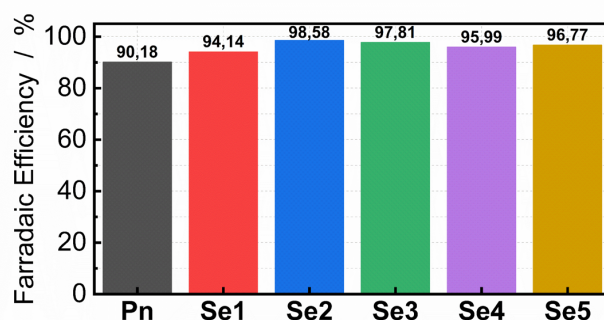
3.4 Faradaic Efficiency

*Figure S10: Faradaic efficiencies of the compounds **Se1** to **Se5** and **Pn**.*

Literature

[1]   B. Konkena, K. junge Puring, I. Sinev, S. Piontek, O. Khavryuchenko, J. P. Duerholt, R. Schmid, H. Tueysuez, M. Muhler, W. Schuhmann, et al., *Nat. Commun.* 2016, *7*, 12269–12277.

[2]   K. junge Puring, S. Piontek, M. Smialkowski, J. Burfeind, S. Kaluza, C. Doetsch, U.-P. Apfel, *J. Vis. Exp.* 2017, *124*, DOI 10.3791/56087.

[3]   C. L. Bentley, C. Andronescu, M. Smialkowski, M. Kang, T. Tarnev, B. Marler, P. R. Unwin, U.-P. Apfel, W. Schuhmann, *Angew. Chem. Int. Ed.* 2018, *57*, 4093–4097.

[4]   R. S. C. Smart, W. M. Skinner, A. R. Gerson, *Surf. Interface Anal.* 1999, *28*, 101–105.

[5]   M. Gui, J. K. Papp, A. S. Colburn, N. D. Meeks, B. Weaver, I. Wilf, D. Bhattacharyya, *J. Membr. Sci.* 2015, *488*, 79–91.

[6]   C. Powell, 1989, DOI 10.18434/T4T88K.

[7]   S. Piontek, C. Andronescu, A. Zaichenko, B. Konkena, K. junge Puring, B. Marler, H. Antoni, I. Sinev, M. Muhler, D. Mollenhauer, et al., *ACS Catal.* 2018, *8*, 987–996.

[8]   I. Zegkinoglou, A. Zendegani, I. Sinev, S. Kunze, H. Mistry, H. S. Jeon, J. Zhao, M. Y. Hu, E. E. Alp, S. Piontek, et al., *J. Am. Chem. Soc.* 2017, 14360–14363.